A Sub-100 μW 0.1-to-27 Mb/s Pulse-based Digital Transmitter for the Human Intranet in 28 nm FD-SOI CMOS

Guillaume Tochou, Robin Benarrouch, David Gaidioz, Andreia Cathelin, Antoine Frappé, Andreas Kaiser, Jan Rabaey

A Sub-100 µW 0.1-to-27 Mb/s Pulse-based Digital Transmitter for the Human Intranet in 28 nm FD-SOI CMOS

Guillaume Tochou, *Graduate Student Member, IEEE,* Robin Benarrouch, *Member, IEEE,* David Gaidioz, *Member, IEEE,* Andreia Cathelin, *Senior Member, IEEE,* Antoine Frappé, *Senior Member, IEEE,* Andreas Kaiser, *Senior Member, IEEE,* and Jan Rabaey, *Life Fellow, IEEE*

***Abstract*—Human body communications require energy-efficient transceivers to connect diverse devices on the human body for wellness and medical applications. This paper presents a fully digital pulse-based transmitter (TX) for capacitive body-coupled communications (c-BCC) in 28 nm FD-SOI CMOS. The transmitter is operating at 450 MHz where surface wave (SW) propagation is the dominant mechanism of capacitive body coupled communication (c-BCC), offering a larger bandwidth with a more stable channel. The heavily duty-cycled transmitter uses a 90 MHz free-running oscillator and edge combiners to generate OOK Gaussian-shaped pulses through a switched-capacitor PA. Wide range forward body-biasing (FBB), specific to FD-SOI technology, allows frequency tuning and adaptive efficiency optimization as a function of data rate. The proposed transmitter consumes 17 to 76 µW for flexible data rates from 0.1 to 27 Mb/s (170 pJ/b down to 2.8 pJ/b) with up to 14 % system efficiency under 0.5 V supply voltage.**

***Index Terms*—Body Area Network (BAN), Ultra-Low Power Transmitter, Ultra-Low Voltage (ULV), Transmitter, Forward Body Biasing (FBB), Body-Coupled Communication (BCC), 28 nm FD-SOI CMOS**

I. Introduction

THE Human Intranet (HI) aims to interconnect various kinds of sensors and actuators on the human body [1]. Such a network is finding applications in wearables and implantable devices for wellness and health purposes such as hearing-aid, continuous glucose monitoring (CGM), electrocardiogram (ECG), oximeter, electromyogram (EMG), brain-machine interface (BMI), among others. In a more long-term view, such a network could possibly become a way to augment ourselves to cope with a quick-changing environment [2].

Today's wearables such as smartwatches and earbuds are usually connected to a smartphone with Bluetooth Low Energy (BLE) technology. This implies a centralized network almost-fully relying on the smartphone which is not robust enough and sensibly limits the battery lifetime to a couple of days. Moreover, BLE technology limits the number of linked devices (up to 7 devices in the latest Bluetooth 5.0 version) and undergoes a limited maximum data rate of 1 or 2 Mb/s. Such data rates are fairly enough for audio and sensor applications (ECG, EMG, etc.) but are too low for more complex applications such as BMI and prosthesis control.

The purpose of the Human Intranet is to create a decentralized network where all types of on-body devices with diverse data rates can interact with each other. For a "user-friendly" experience, the devices need to have a small form-factor for comfortable wearability. To avoid battery replacement or allow battery-less devices, the power consumption has to be as low as possible for a long-term operating life. It is also required to reach "long-range" (at the human body scale) communication to avoid the use of repeaters that would degrade the wearability and power consumption of the network. Finally, the network requires a robust communication scheme when undergoing changing environments and motions. We can then identify 5 main requirements for the design of Human Intranet transceivers :

- Flexible data rate
- Wearability/Form factor
- Power consumption/Energy efficiency
- Range/Body coverage
- Robustness

On a higher level, it is important to note that privacy, security, and safety cannot be neglected at any cost [3].

In [4] a decentralized network topology was proposed. It presents a "mesh-of-star" topology where *Hubs* are interconnected with each other in a mesh topology and the *Leaves* are connected in a star topology with a *Hub* as the local central node (Fig. 1). *Hubs* are defined as the nodes generating an important amount of data (e.g. BMI, prosthesis control, etc.), with low latency and more computing capability, embedded intelligence, and available energy. On the other hand, *Leaves* are defined as nodes generating a lower amount of data, such as temperature and chemical sensors, ECG, etc., and are

Manuscript received XXX X, XXXX; revised XXX XX, XXXX; accepted XX XX, XXXX. Date of publication XXX XX, XXXX; date of current version XX X, XXXX.

G. Tochou and R. Benarrouch are with STMicroelectronics, Crolles France ; Univ. Lille, CNRS, Centrale Lille, Junia, Univ. Polytechnique Hauts-de-France, UMR 8520 - IEMN – Institut d'Electronique de Microélectronique et de Nanotechnologie, F-59000 Lille, and Berkeley Wireless Research Center, UC Berkeley, CA, USA (guillaume.tochou, robin.benarrouch@st.com)

A. Cathelin and D. Gaidioz are with STMicroelectronics, Crolles, France (andreia.cathelin, david.gaidioz@st.com)

A. Frappé and A. Kaiser are with Univ. Lille, CNRS, Centrale Lille, Junia, Univ. Polytechnique Hauts-de-France, UMR 8520 - IEMN – Institut d'Electronique de Microélectronique et de Nanotechnologie, F-59000 Lille (antoine.frappe, andreas.kaiser@junia.com)

J. Rabaey is with Berkeley Wireless Research Center, UC Berkeley, CA, USA (jan_rabaey@berkeley.edu)

Color versions of one or more of the figures in this letter are available online at http://ieeexplore.ieee.org.

Digital Object Identifier XXXXXXXXX

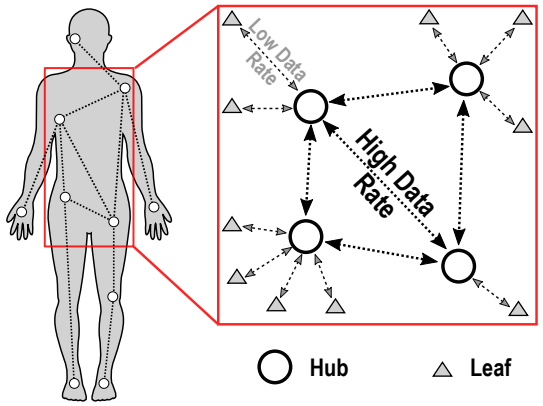

Fig. 1. The Human Intranet network [4].

much more energy-constrained. Hence, *Hubs* require a high communication data rate (tens of Mb/s) where *Leaves* require lower data rates (hundreds of kb/s) to save power.

This work presents an ultra-low power transmitter suitable for both *Hubs* and *Leaves* with a flexible data rate for the Human Intranet. This paper presents an extended version of [5]. The paper is structured as follows : Section II presents the state of the art in Body Area Network (BAN) and how the different existing solutions cope with the requirements stated in the introduction. Section III presents the system principles of the proposed transmitter. Section IV describes the circuit implementation. Section V presents the measurement results and compares this work with the state of the art. Section VI presents the on-body demonstration of the propagation mechanism with the transmitter. Finally, Section VII concludes this work.

II. State of the Art in Body Area Network

A. Free-space RF communication

As stated in the introduction, BLE is a very widely used standard making the devices easily compatible one with another, but suffers from limited data rates and most of the time with important power consumption [6], [7]. Another extensively studied solution using RF propagation for BAN is Ultra-Wideband (UWB). The principle of UWB lies in a pulse-based communication in the $3.1-10.6$ GHz band. Each bit is transmitted by a short-time pulse allowing bit-level duty cycling for reduced power consumption, especially at low data rates. Simple modulations are usually used such as OOK, PPM, and BPSK. OOK and PPM allow using non-coherent receivers reducing the constraints and power consumption by using a PLL-free architecture. This communication technology has demonstrated its ability to reach high data rates and its energy efficiency [8]–[13].

However, communicating over the air around the human body is challenging because of the *body shadowing* effect. When communicating on-body or around-body, the human body absorbs the radio signal when the transmitter and the receiver are non-line-of-sight (e.g. for a torso to back communication). This degrades the path loss and makes the channel unstable with motion and varying environments. To compensate for the body shadowing effect, it would require increasing the output power of the transmitter, improving the sensitivity of the receiver, using larger gain antennas, and/or using repeaters. Such solutions would inevitably increase the power consumption and/or downgrade the wearability of the nodes.

B. In-Body Ultrasound

As the human body is mostly composed of water ultrasounds propagate easily in the human body. Hence this communication technique has been recently studied for human body communication. However, the channel suffers from multipath caused by the reflections of the heterogeneous medium composed of muscle, bone, and skin material [14]. Furthermore, similarly to electromagnetic communication, losses increase with the frequency which limits the central frequency of the transducers to $\sim$10 MHz. This frequency limitation inherently restrains the bandwidth and hence the communication data rate [14]. Ultrasound remains a good communication option for short-range implant (under-skin) to on-body (on-skin) communication with a low data rate.

C. Body Coupled Communication

To overcome the body shadowing effect, a recently studied alternative solution is body coupled communication (BCC). This solution proposes to use the human body as the communication channel instead of free-space. Three different mechanisms have been mainly studied so far in BCC [15] :

1) Magnetic BCC (m-BCC): This mechanism is using resonant coils wrapped around body limbs to communicate through magnetic fields. Magnetic fields travel with low loss through biological tissue, as the human body is magnetically inert [16]. Hence, if the magnetic resonance is kept constant, magnetic coupling reaches low path loss with all body coverage. This allows reaching ultra-low power transceivers with low output power at the TX side and relaxed sensitivity at the RX side [17]. However, coils wrapped around the body are not easily wearable. For example, having a coil around the head or the torso is not convenient. Furthermore maintaining magnetic resonance is easily sensitive to motion artifacts. It remains a good communication option if both the receiver and transmitter are on the same limb with light coils.

2) Galvanic BCC (g-BCC): This communication scheme uses two electrodes on both the transmitter and the receiver. The principle is based on a differential signal creating a galvanic current propagating thru the skin. Galvanic coupling has the advantage to be very robust to environment changes due to a very stable channel. However, it suffers from strong path loss beyond a few centimeters [18]. Furthermore, the low frequency of operation limits the usable bandwidth and hence the data rate. Thus, this makes g-BCC a good candidate for an implant (under-skin) to on-body (on-skin) communication, but makes full-body coverage communication unachievable.

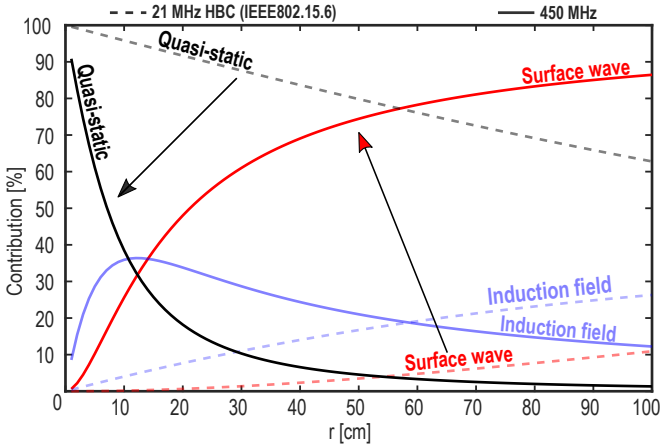

Fig. 2. Contribution of each mechanism as a proportion of the total electric field for 21 MHz (dotted lines) and 450 MHz (solid lines).

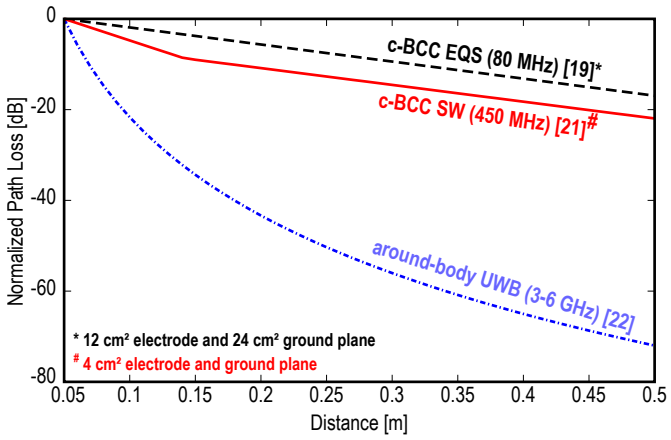

Fig. 3. Channel model of c-BCC SW [21] compared to c-BCC EQS [19] and around-body UWB [22] (Note: The path loss models are normalized at 5 cm distance from the antenna/electrode as the insertion loss depends on the antenna/electrode impedance matching).

3) Capacitive BCC (c-BCC): the principle is based on one electrode in contact with the skin at the TX and RX side, with a floating electrode on each side acting as ground electrodes. The signal propagates along the body as an electric field. The return path is formed by the ground and air environment creating a capacitive coupling between the transmitter and the receiver [19]. The dominant propagation mechanism in capacitive body coupled communication depends on two parameters : frequency and distance (Fig. 2). For a higher frequency and/or longer distance the dominant propagation mechanism is the surface wave (SW) propagation. On the other hand, at a lower frequency or very short distances, electro quasi-static (EQS) coupling will be the dominant mechanism. c-BCC with a frequency of operation below 100 MHz offers low path loss for a distance up to 1.5 m [19]. However, because of the important influence of the return path on the channel, the communication can be sensitive to changing environment and motion when EQS is the dominant propagation mechanism.

Capacitive body-coupled communication in the 400−500 MHz band has been studied in [20], [21], with the main idea to increase the carrier frequency and the available bandwidth and hence the data rate. At 450 MHz the path loss can be approximated with EQS near-field propagation for up to 15 cm. At a further distance, surface wave propagation becomes predominant and the path loss is approximated by far-field propagation (Fig. 2). [21] demonstrated with numerical simulation and measurements that far-field losses have a slope of −0.37 dB/cm at 450 MHz which is approximately the same slope value of a near-field EQS propagation at 80 MHz found in [19]. The two models: EQS propagation at 80 MHz and surface wave model at 450 MHz are compared in Figure 3. These two models are also compared to a UWB around-body model [22] to emphasize how UWB, and more generally over-the-air radio transmissions, suffers from the body shadowing effect, causing important path loss compared to c-BCC. The path loss models are normalized at 5 cm distance from the antenna/electrode as the insertion loss (loss at 5 cm distance) depends on the antenna/electrode impedance matching. Furthermore, [21] highlighted a minimum available bandwidth of 100 MHz at 450 MHz over which the attenuation is almost to be constant. Ultimately, since the propagation mechanism is dominated by surface waves phenomena at 450 MHz, a system implementation at this frequency of operation enables a communication less sensitive to environment changes since the return path has almost no impact at this frequency of operation [21].

Several transceiver implementations have been proposed in the state of the art using capacitive body coupled communication [23]–[29]. All of them use frequencies below 150 MHz where the EQS propagation mechanism is predominant. [23], [24] proposed transceivers with direct-baseband communication with up to 30 Mb/s and 150 Mb/s, respectively. Such solutions allow using simple driving buffers at the transmitter side and defer the complexity to the receiver. Although both solutions report good energy efficiency below 20 pJ/b, the reported power consumption does not take into account the clock generation power consumption which would be the most power-consuming part. [27], [28] proposed transceivers compliant with the IEEE 802.15.6 BAN standard section dedicated to human body communication [30]. In this standard section, the frequency of operation is defined at 21 MHz with a 3 dB bandwidth of 5.25 MHz with a constrained mask-shaping requiring a sharp rejection below 2 MHz [28]. Such low frequency of operation and bandwidth limits the maximum achievable data rate to a few Mb/s. [29] proposed a dual-transceiver being able to communicate efficiently at both high (80 Mb/s) and low data rate (100 kb/s). The high data rate transceiver uses a dual-band communication with BPSK modulation in the 20−60 MHz and 140−180 MHz bands to avoid FM-band interference (80−100 MHz).

III. System Considerations of the Proposed Transmitter

According to the channel studies in the 400−500 MHz band [20], [21], this allows for wide bandwidth >100 MHz

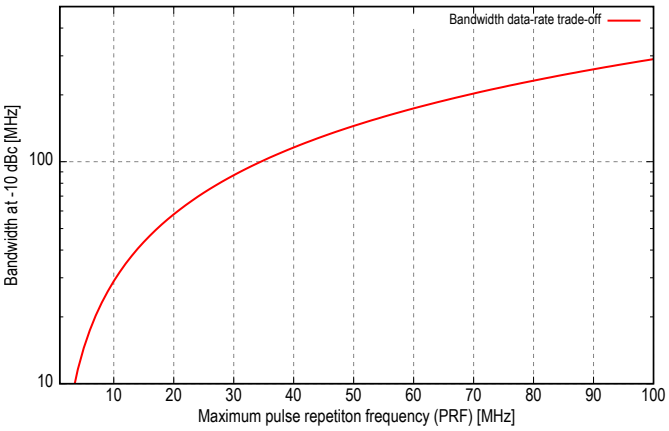

Fig. 4. Maximum pulse repetition frequency (i.e. maximum data rate) versus bandwidth trade-off.

and more channel stability under motion and changing environment. Taking advantage of the wide available bandwidth, the TX is inspired by UWB principles with the use of pulse-based communication with simple OOK modulation. Pulse-based communication can handle aggressive duty-cycling transmitters allowing for low power consumption and the ability to reach high data rates. From the analysis in [31], the trade-off between bandwidth (BW) and maximum data rate is defined. The temporal expression of a pulse centered at the frequency f_c with a Gaussian envelope can be written as:

$$p(t) = A \exp\left(-\frac{t^2}{2\sigma^2}\right) \cos(2\pi f_c t) \tag{1}$$

where A is the maximum amplitude of the pulse and σ the standard deviation of the Gaussian envelop. In the frequency domain the single side-band Fourier transform of (1) gives:

$$P^+(f) = A\sqrt{\pi}\sigma \exp\left(-\frac{(2\pi\sigma(f-f_c))^2}{2}\right) \tag{2}$$

The trade-off between the pulse width ($T_p =\sim 6\sigma$), and hence the maximum pulse repetition frequency ($PRF =\sim 1/6\sigma$), and the bandwidth (BW) at -10 dBc is given by solving :

$$10\log_{10}\left(\frac{|P^+(f)|^2}{|P^+(f_c)|^2}\right)\Bigg|_{f=f_c\pm BW/2} = -10\ dB \tag{3}$$

This gives the following relationship between BW and PRF:

$$BW(PRF) = \frac{\sqrt{-\ln(0.1)}\cdot PRF}{\pi} \tag{4}$$

This function is plotted in Figure 4. As a compromise between available bandwidth and maximum achievable data rate, the chosen bandwidth is 150 MHz, which corresponds to a ∼20 ns pulse. For a 1 bit per pulse modulation like OOK, this is corresponding to a maximum theoretically achievable data rate of ∼50 Mb/s. A shorter pulse would require more bandwidth, while a longer pulse would limit the maximum achievable data rate. Furthermore, as OOK modulation does not require specific phase noise requirements as it is an amplitude modulation, short pulses with this simple modulation enable the use of an unlocked free-running oscillator, avoiding the use of a PLL which is a power-consuming part in RF circuits.

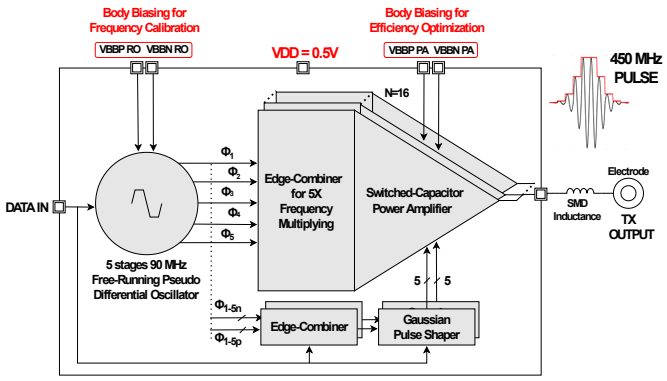

Fig. 5. Proposed architecture of the c-BCC SW TX.

The chosen frequency is not covered by the IEEE 802.15.6 standard for c-BCC communication, hence there is no specific spectrum mask to fulfill. However, as the fractional bandwidth is more than 20 % we can consider the signal as a UWB signal, which should respect FCC regulation [32]. Although the emitted signal would be mainly confined to the body, the signal will partially radiate because of the *body antenna effect*, where the human body acts as an antenna radiating the signal power into the air [33]. The impact of the body antenna effect has not been measured yet for frequencies higher than 150 MHz, but this effect is expected to increase with frequency. Hence, it is desirable to limit out-of-band emissions, for example in the GPS band (960−1610 MHz) [32].

The transmitter has been designed for a 50 Ω load for measurements purposes. In a complete solution, specific electrodes matched to the desired impedance should be designed. Regarding the receiver requirements, these have been addressed in [4]. From the system analysis with classical RF models, it is estimated that a receiver with a sensitivity of −104 dBm and −77 dBm, at low and high data rates respectively, would allow for communication up to 50 cm on-body.

IV. Transmitter Implementation

The proposed TX circuit (Fig. 5) is composed of a free-running pseudo-differential ring oscillator (PD-RO) at 90 MHz feeding a switched-capacitor power amplifier (SCPA) with embedded edge-combiners (EC), in order to reach the 450 MHz central frequency. The overall TX is data-enabled (OOK modulation), which means it only runs during the pulse duration, saving power at low data rates. Short pulses combined with non-coherent OOK modulation accept the use of an unlocked frequency reference and enable instant startup time and aggressive duty-cycling. A low-frequency oscillator with frequency multiplication in the power amplifier allows for reduced dynamic power consumption as the circuit is massively low-frequency operated. Digital pulse-shaping is also introduced for spectral efficiency limiting out-of-band emissions. The 28 nm FD-SOI technology allows for threshold voltage tuning through wide range body-biasing. As depicted in Figure 6, in the 28 nm FD-SOI technology, the body factor is ∼85 mV/V for the thin oxide LVT devices and the body

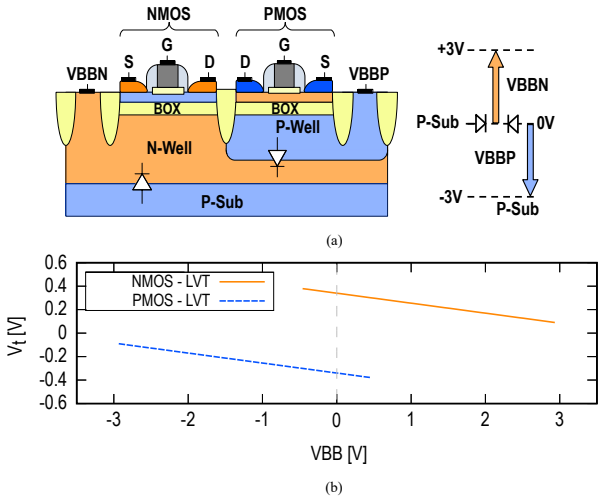

Fig. 6. (a) FD-SOI cross section and body-bias range (b) LVT NMOS/PMOS threshold voltage versus body-bias voltage.

voltage variation can range up to +/- 3 V [34]. This feature is used in three folds in the proposed circuit. First, it enables low threshold voltage allowing ultra-low voltage operation down to 0.5 V for ultra-low power consumption. Secondly, it allows for frequency calibration and process compensation on the oscillator, by tuning the threshold voltage of the inverters in the ring oscillator. Thirdly, it enables power amplifier efficiency optimization by reducing the ON-resistance of the transistors. The oscillator's and SCPA's output inverters are custom designed with a gate length increased to L_{min} + 16 nm as well. This relaxed gate length limits the impact of leakage and offers manufacturing robustness while operating at 0.5 V.

The one-time calibration, through body-biasing, of the PD-RO and the EC-SCPA is made externally. In future work, a complete SoC implementation with integrated body-bias generator [35] and periodic calibration with an on-chip reference should be designed. Such additional parts will certainly add power consumption overhead to the transmitter. However, an integrated body-bias generator would allow to duty-cycle the body-biasing by the input data like the rest of the transmitter. Hence, it will decrease the static power consumption due to leakage currents. Similarly to the body-bias generator, voltage regulation shall be included in a complete SoC implementation.

A. Pseudo-Differential Ring Oscillator

A ring oscillator requires at least two periods to oscillate. Hence, the 90 MHz frequency is chosen as two periods correspond to 22.22 ns which is the specified pulse width. A pseudo-differential architecture is composed of two single-ended ring oscillator loops mounted in a pseudo-differential topology using inverter-based latch locking between each stage. The PD-RO circuit is represented in Figure 7. The oscillator is based on 45 stages pseudo-differential architecture. 5 phases are taken every 9 stages from both the negative and positive loops to perform frequency multiplication. The PD-RO is designed with an important number of stages to reach

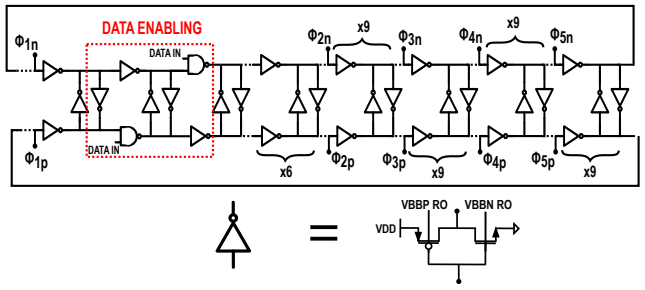

Fig. 7. 90 MHz Pseudo-differential Ring-Oscillator (PD-RO) schematic.

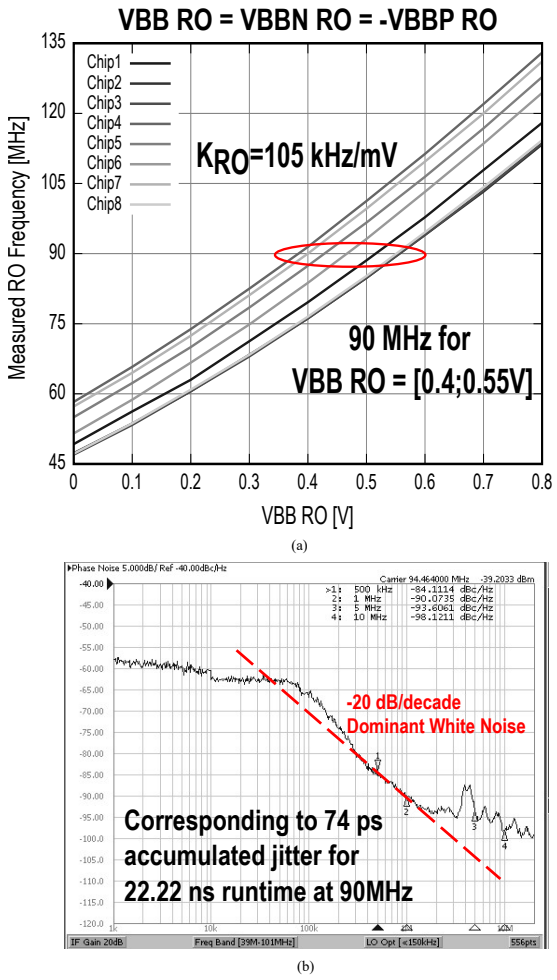

Fig. 8. (a) Measured PD-RO Frequency vs body-bias voltage for 8 devices (b) PD-RO phase noise measurement (the plateau from 1 kHz to 100 kHz is due to the internal PLL of the measurement equipment locking).

low-frequency of oscillation and to enable symmetric duty-cycling for proper edge-combining. The positive feedback enables fast current transitions with sharp edges as required for the edge combination [36]. A NAND gate inside each loop duty-cycles the oscillator according to the input data.

The PD-RO low-frequency reduces the power consumption of the frequency reference down to 11 μW when running at 90 MHz. As presented in Figure 8.a, the oscillator frequency fine-tuning is obtained via body-biasing through a one-time calibration (around VBB_{RO} = 0.5 V), and to compensate

process variations between different devices. As the PD-RO is turned-off between each pulse by the introduced NAND gates, there is no long-term drift of the oscillator. According to jitter theory in free-running ring oscillator, for a short runtime, white noise is the dominant noise source in free-running oscillators, and jitter increases as the square root of the run-time [37]. Hence by measuring the phase noise of the oscillator in the -20 dB/decade slope the equivalent accumulated jitter can be calculated. In Figure 8.b we present the measured PD-RO phase noise. The PD-RO achieves a measured accumulated jitter of 74 ps when running for a 22.22 ns duration.

B. Edge-Combiners Switched-Capacitor Power Amplifier

As presented in Figure 9.a and 8.c the edge-combiners (EC) are performing frequency multiplication by 5 to reach the 450 MHz central emission frequency. In each SCPA slice, an edge combiner multiplies the PD-RO frequency by using the 5 phases of the 90 MHz oscillator. Having the edge combiner distributed in each of the 16 slices allows having the 450 MHz frequency only at the very final inverter of each slice allowing a massively low-frequency operated circuit. It also relaxes the constraints on buffers and 'clock' tree distribution, with the multiplication performed only in the activated slices. In practice, the conceptual AND and OR gates represented in Figure 9.a are implemented in NAND logic for fast switching, limiting the introduced jitter by the edge-combiners. As observable in Figure 11, the edge-combiners provide robust frequency-multiplication thanks to body-biasing. Applying a 2.2 V body biasing on the edge-combiners reduces by 40X the standard deviation of process and mismatch variations compared to a nominally body-biased edge-combiner. This effect is explained by the threshold voltage reduction offered by FBB, making the switching of the NAND gates sharper and hence reducing timing errors.

The edge combiner drives an output inverter in series with a 135 fF capacitance acting as a switched capacitor power amplifier. CMOS inverter-based SCPA allows for high integrability, digital configuration, and high efficiency [38]. The energy-efficiency of an SCPA strongly depends upon the ON-resistance (r_{on}) of the switches in the output inverters. The usual technique to reduce r_{on} is to increase the width of the transistors. However, this leads to an increase of the parasitic capacitance, increasing the dynamic power consumption and hence degrading the efficiency of the power amplifier. The forward body-biasing (FBB) knob, specific to FD-SOI technologies, is used to lower the threshold voltage of the transistors, reducing r_{on} at the low 0.5 V supply voltage, limiting their size and parasitic capacitance which improves the efficiency of the power amplifier as well as saving area. By using the simulation-validated model proposed in [39] it is shown in Figure 10 that a forward body-biased SCPA improves by 6 % the peak system efficiency (SE_{peak}) of the power amplifier while reducing by 45 % the switches area at 450 MHz. For further area saving the unit capacitances C_u in each slice are MOM capacitances stacked on top of the inverters.

From SCPA theory [38], for an ideal peak output power of 0 dBm and a supply voltage of 0.5 V, the optimal load is equal

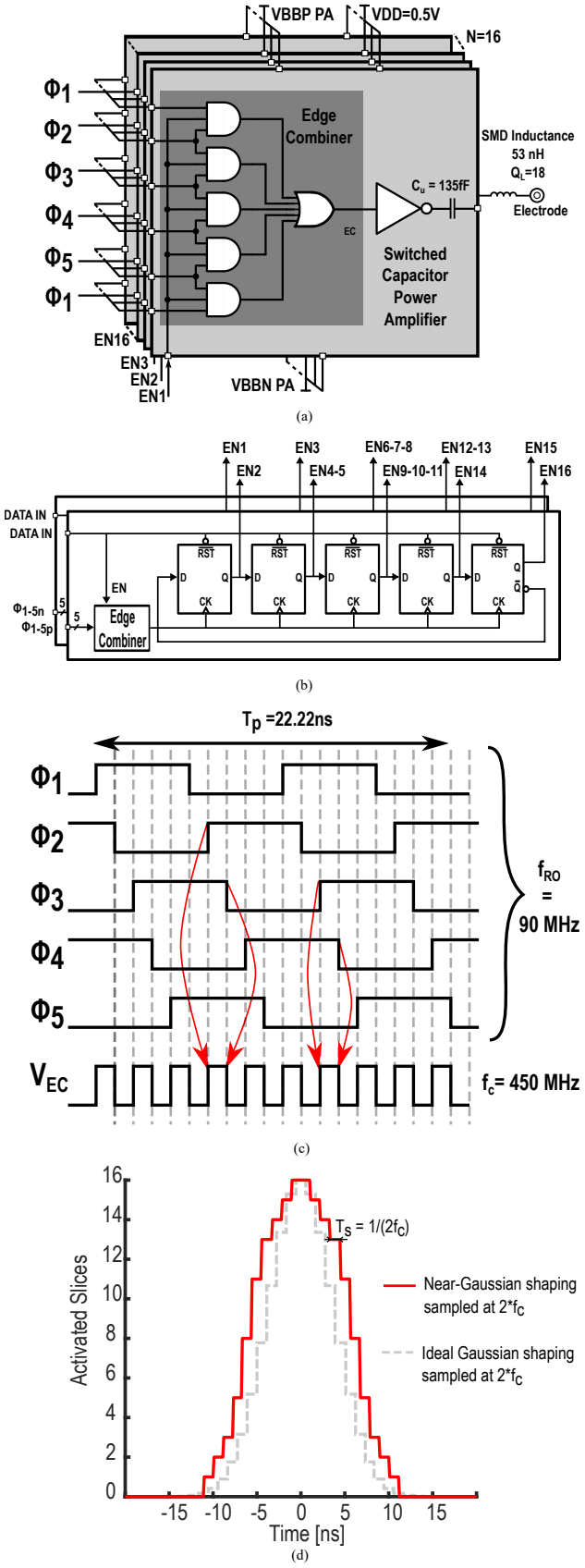

Fig. 9. (a) Schematic of the EC-SCPA (b) Schematic of the digital pulse shaper (c) Timing diagram of the EC (d) Gaussian pulse envelop generated by the pulse shaper.

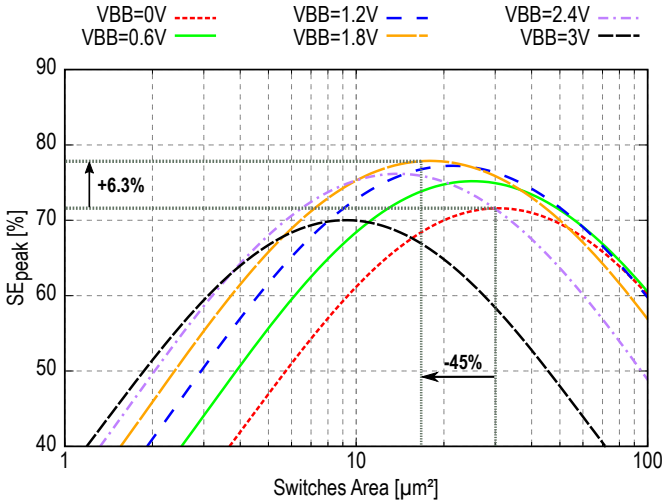

Fig. 10. Model of the peak system efficiency (SE) of a SCPA at 450 MHz for different body-biasing values (Switches Area for an optimal load of 50 Ω).

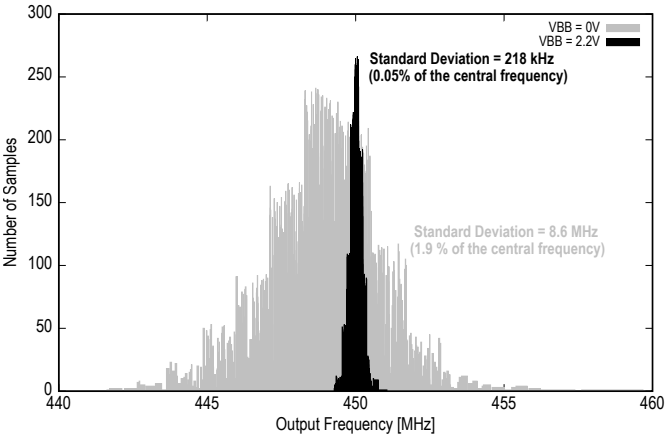

Fig. 11. Monte-Carlo simulations (process and mismatch) of the Edge-Combiner for 1000 iterations with nominal body-biasing (light grey) and 2.2 V body-biasing (black).

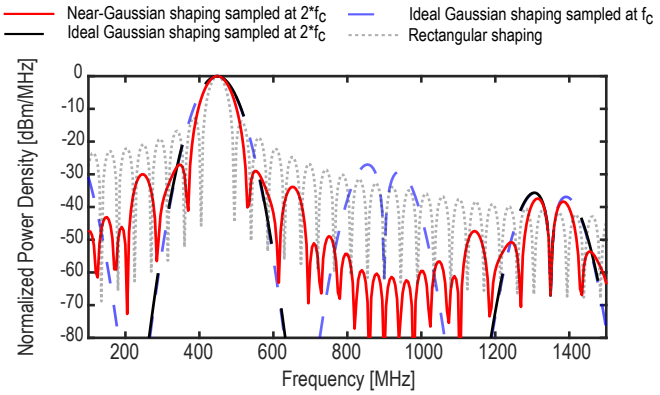

Fig. 12. Impact of pulse shaping waveform on the frequency response.

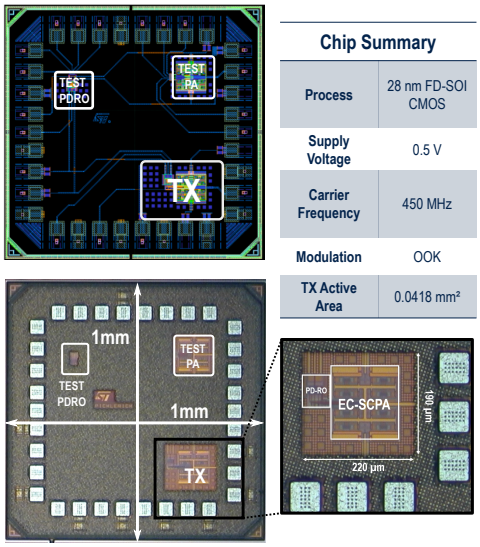

Fig. 13. Chip summary with die photograph and layout.

to 50 Ω which avoids the use of a lossy matching network. An external inductance is used in a 0402 package to form a wideband LC bandpass filter centered at 450 MHz.

C. Digital Pulse Shaping

As observable in Figure 12, the pulse shape has an important impact on the frequency response of the transmitter. With a rectangular pulse shaping (i.e. no pulse shaping) important sidelobe emissions are observable which cause interferences and degrade spectral efficiency. Gaussian pulse shaping has already been demonstrated to be very efficient to limit out-of-band spectral emissions [8], [31]. Similarly to [8], Figure 12 compares ideal Gaussian pulse shaping with sampling frequencies equal to f_c and $2f_c$. It is shown that an ideal Gaussian pulse shaping at $2f_c$ sampling frequency removes the sidelobes emissions at $2f_c$, limiting out-of-band emissions. Hence, a near-Gaussian pulse shaping, as shown in Figure 9.d, with a sampling frequency of $2f_c$ is implemented. In Figure 9.b the schematic of the implemented pulse-shaper is presented. A dual 5-bit Johnson ring counter driven by complementary clocks provides the enable (ENx) signals. The complementary 450 MHz clocks are generated by two identical edge combiners from respectively the positive and negative phases of the 90 MHz PD-RO (ϕ_{1-5n}, ϕ_{1-5p}). The $2f_c$ frequency is then easily generated without power consumption overhead by using the complementary clocks, thanks to the pseudo-differential architecture of the oscillator. The frequency response of the near-Gaussian pulse shaping implemented is observable in Figure 12, and shows that it limits out-of-band emissions at $2f_c$ frequency and improves spectral efficiency. The pulse shaper and edge combiners are designed using standard cells with a poly-biasing (i.e. gate length extension) of 16 nm. The digital pulse-shaper, edge-combiners, and associated logic are body-biased with the same voltage as the power amplifier (VBB_{PA}) for fast-switching at low operating voltage.

V. Measurements Results

The presented chip has been implemented in the 28 nm FD-SOI CMOS technology from STMicroelectronics, as presented

TABLE I
STATE OF THE ART COMPARISON FOR BAN TX

	This Work		H. Cho [29] JSSC'15		J. Lee [24] VLSI' 17	W. Saadeh [25] JSSC' 17	J. Jang [26] JSSC' 19	S. Maity [23] JSSC'19	B. Chatterjee [27] RFIC' 20		J. Park [17] JSSC'19	G. De Streel [8] JSSC'17		X. Chen [6] JSSC' 19	Y. Shi [7] ISSCC' 19
Radio Technology	**C-BCC (SW)**		C-BCC (EQS)		C-BCC (EQS)	C-BCC (EQS)	C-BCC (EQS)	C-BCC (EQS)	C-BCC (EQS) IEEE 802.15.6		M-BCC	UWB IEEE 802.15.4a		BLE	BLE
Process Technology	**28nm FD-SOI**		65nm		65nm	65nm	65nm	65nm	65nm		65nm	28nm FD-SOI		40nm	65nm
Carrier Frequency [MHz]	**350 - 550**		13.56	20 - 60 140 - 180	Baseband <100MHz	20 - 120	20 - 60 100 - 180	Baseband <100MHz	22.27		40	3500 - 4500		2400	2400
Supply Voltage [V]	**0.5**		1.2	1	Not Reported	1.1	1	1	0.7		0.6	0.55		0.6	1.2
Data rate [Mb/s]	**0.1**	**27**	0.1	80	100	2	80	30	1	10	5	0.11	27	1	1
Modulation	**OOK**		OOK	BPSK	Decision Feedback Equalization	P-OFDM BPSK	QPSK BPSK	NRZ	OOK		OOK	BPM/BPSK		GFSK	GFSK
TX Power Consumption [µW]	**17**	**76**	21	2600	350*	870	1700	93*	20.6	22.4	37	100	380	490	610
TX Energy per bit [pJ/b]	**170**	**2.8**	210	32.5	3.5	435	22	3.1	20.6	2.24	7.2	950	14	490	610
Output Power [dBm]	**−33.8**♯	**−19.7**♯	Not Reported		Not Reported	Not Reported	Not Reported	Not Reported	Not Reported		−24.8	−20		−19	−8.4
TX System Efficiency [%]	**2.44**	**14**	Not Reported		Not Reported	Not Reported	Not Reported	Not Reported	Not Reported		17.8	2.6		2.6	23.6
Area [mm²]	**0.0418**		0.1672	5.76	0.00348	0.54	1.3	0.02	0.117		0.0204	0.095		0.0166	0.494

♯ Note: For a 50 Ω load * Note: Not including frequency synthesis power consumption

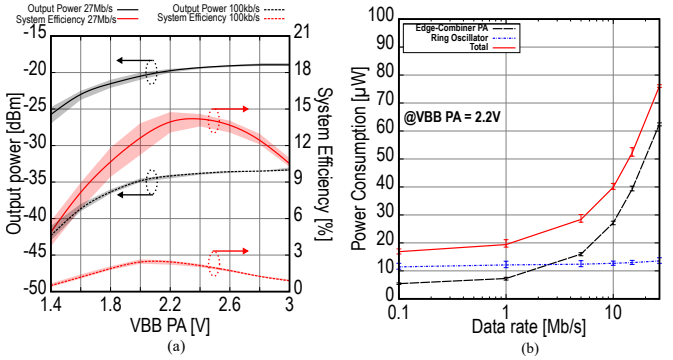

Fig. 14. (a) Average output power and System Efficiency versus body-biasing voltage for different data rate (Lines represent the average measured values and the shaded curves represent the boundaries of minimum of maximum measured values on several devices) (b) Power Breakdown of the TX at VBB_{PA} = +/- 2.2 V versus data rate (error bars represent the boundaries of minimum of maximum measured values).

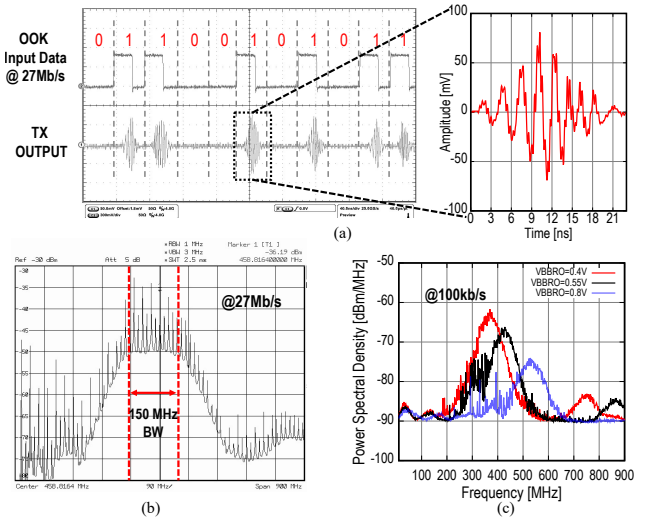

Fig. 15. (a) Timing response of the TX at 27 Mb/s. (b) Spectrum response at 27 Mb/s. (c) Frequency response for different body bias voltage on the ring oscillator at 100 kb/s.

in Figure 13. For measurements, LDOs are placed on PCB for voltage regulation at 0.5 V. The proposed transmitter reaches a maximum achievable data rate of 27 Mb/s. The output power and system efficiency of the TX is measured on several devices at the maximum data rate (for Hub-to-Hub communication) and at a low data rate of 100 kb/s (for Leaves to Hub communication). In Figure 14.a the output power and system efficiency (at low and high data rates) is plotted versus the applied body-biasing voltages on the power amplifier. It shows that for a measured −19.7 dBm output power at the maximum data rate of 27 Mb/s, the EC-SCPA reaches an optimal operating point at VBB_{PA} = 2.2 V where the system efficiency is maximum reaching 14 %. An optimal body biasing point exists as FBB decreases the ON-resistance, while on the other hand, it increases the current leakage. Hence, the optimal bias corresponds to the point where the leakage power consumption becomes predominant. The body-biasing voltage can be adapted to reach the best system efficiency for a given data rate, or to compensate process variations, through one-time calibration. The TX consumes 76 μW at 27 Mb/s, which corresponds to an energy efficiency of 2.8 pJ/b, for an overall 14 % system efficiency at −19.7 dBm average output power. For the lowest data rate (100 kb/s), the TX consumes 17 μW with 2.44 % system efficiency, translating into an energy efficiency of 170 pJ/b for a −33.8 dBm average output power. The output power is measured for a 50 Ω load, impedance of the measurement equipment. The power breakdown of the transmitter is plotted versus the data rate in Figure 14.b. The PD-RO is the dominating power consumer for a data rate up to 2 Mb/s because of its static power dissipation. At higher data rates the EC-SCPA becomes the largest power-consuming part of the TX. Figure 15 shows the OOK modulated output signal in the time and frequency domains for the low and high data rates (100 kb/s and 27 Mb/s) and highlights the large signal

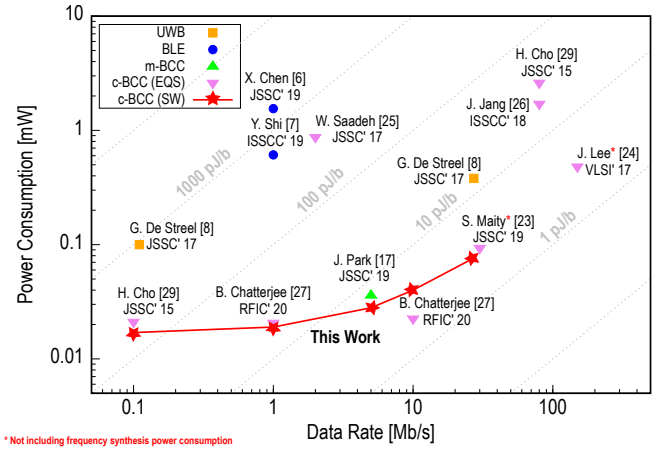

Fig. 16. Power consumption versus data rate compared with TX state of the art.

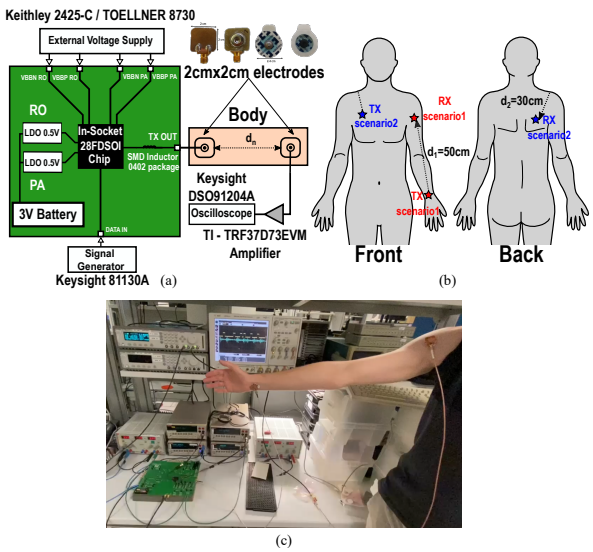

Fig. 17. (a) Set-up for on-body demonstration (b) Scenarios for on-body demonstration (c) Picture of the body-coupled demonstration on the arm.

bandwidth and the effect of the pulse shaping. We can notice in Figure 15.b spurs spaced by 27 MHz which corresponds to the pulse repetition rate. However, the frequency response is better at $f_c \approx 350$ MHz (VBB_{RO} = 0.4 V) as observable in Figure 15.b. This is due to a slight mismatch of the LC filter at the output, because of parasitics. A slight change of the LC bandpass could result in a performance improvement in terms of output power and efficiency at 450 MHz and remove the spurs in the 300−400 MHz band. The pulses reach a peak-to-peak amplitude of ∼150 mV. The pulses amplitude remains constant at any data rate, which automatically scales the average output power with data rate. The active area of the TX occupies 0.0418 mm² (Fig. 13).

The TX performances are summarized in Table I and compared with state of the art transmitters for BAN. For a visual comparison of the TX performances, the total power consumption is plotted versus the data rate and compared with state of the art TXs in Figure 16. The power consumption of the surface-wave transmitter is at par or better than the state-of-the-art over the full range of data rates. When compared to UWB TX, this work shows a ∼5X improvement in energy efficiency at both high and low data rates for similar output power [8] without suffering from the body shadowing effect. Compared to m-BCC [17] the TX achieves a 20% reduction in power consumption at an equal data rate (5 Mb/s) with similar output power. With respect to a c-BCC (EQS) TX [29], this SW solution improves the energy efficiency by 11X and 1.2X, for the high and low data rates, respectively over the state-of-the-art. In comparison with [27], this work offers a wider range of operating data rate and a higher maximum achievable data rate with equivalent energy efficiency order. [23] also reports a 30 Mb/s transmitter with similar energy efficiency (∼3pJ/b) but does not take into account the power consumption of the clock generation, which can easily be predominant in such low power circuits. Similarly, [24] reaches a very high data rate up to 150 Mb/s with 3.5 pJ/b energy efficiency but does not take into account the power consumption of the frequency synthesis. Finally, [26] also reports a very high data rate up to 80 Mb/s but at the cost of a 22X higher power consumption.

The key techniques to reach state-of-the-art energy efficiency are: 1) ultra-low voltage operation enabled by body-biasing 2) pulse-based communication for high duty-cycling 3) massively low-frequency operated architecture to reduce dynamic power consumption.

VI. On-Body Demonstration

Finally, as a proof of concept, a demonstration of the signal propagation on the human body is shown in Figure 17. On-body measurements are challenging for c-BCC because the ground planes must be considered carefully [33]. The transmitter is battery powered to avoid earth-grounded supply but the PCB-ground remains large and the amplifier at the RX side has a earth-grounded power supply. Although using SW as the dominant propagation mechanism limits the impact of the return path by nature, it should still be noted that such a setup is not fully representative of a communication between on-battery wearable devices with small ground planes. The signal propagation is demonstrated in two scenarios. The first scenario (in red in Figure 17) demonstrates a communication along the arm where the two electrodes are in line-of-sight with a distance up to 50 cm. In the second scenario (in blue in Figure 17), one electrode is placed on the pectoral while the second is placed on the shoulder blade. In this scenario, the electrodes are non-line-of-sight and spaced from each other at a distance of 30 cm (following the path along the body). This second scenario helps to demonstrate the capabilities of body coupled communication when undergoing the body shadowing effect. A 4 cm² electrode (similar to the one used in [21]) is wired to the output of the battery-powered TX and attached to the body. As a receiver, a TRF37D73EVM amplifier from Texas Instruments, offering a 20 dB gain, is attached to a second electrode with the same dimensions. The signal is then observed and recorded on a digital oscilloscope from Keysight (DSO91204A). In Figure 18 post-measurement signal processing is applied on

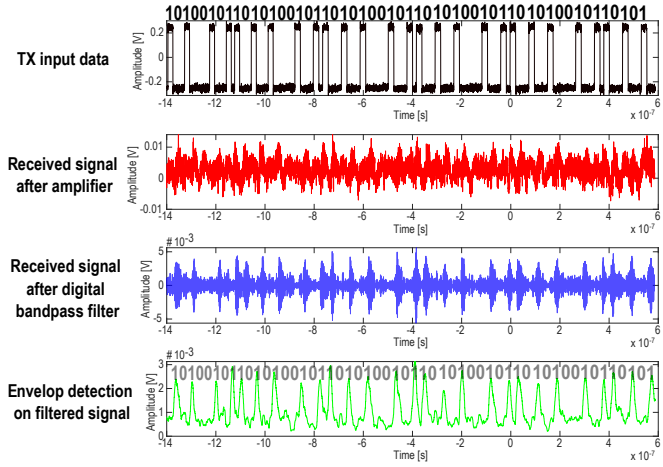

Fig. 18. Signal processing on the measured received signal for the pectoral to shoulder scenario (blue in Figure 17).

the measured received signal. After applying a digital band-pass filter and envelope detection, the data can be easily retrieved. Furthermore, it is notable that when the electrodes are not attached to the body (air propagation) the signal is merely observable over a few centimeters. This demonstrates that the mechanism of propagation is truly body-coupled and not because of the electrodes acting as antennas with over-the-air propagation. A video of the full demonstration is available at [40].

VII. Conclusion

A 0.5 V 28 nm FD-SOI CMOS ultra-low voltage transmitter with flexible data rate (100 kb/s to 27 Mb/s) and using capacitive body-coupled communication with surface wave propagation is presented. The highly duty-cycled transmitter with pulse-based communication uses a low frequency, body-bias controlled oscillator and a switched-mode power amplifier with embedded frequency multiplier, Gaussian pulse shaping, and body-bias efficiency optimization. When compared to body-coupled transmitter state of the art, the proposed TX solution shows better flexibility as addressing a wider operation data rate, while staying at par or better in terms of energy efficiency. Moreover, the surface wave body-coupled link has been successfully demonstrated on-body using an off-the-shelf receiver. Future work will focus on the design of 1) a fully integrated solution with on-chip body-bias generation and periodic calibration, 2) the design of a receiver to demonstrate a full data transfer on-body, 3) electrode design with emerging flexible electronics and proper impedance matching, 4) and implementation of the MAC protocol [4] for a full demonstration of the HI network [41].

Acknowledgment

The authors would like to thank Arno Thielens, Matthew G. Anderson, Ragnvald Nicolas Bernt and Matias Rietig for helpful discussions.

References

[1] J. M. Rabaey, "The Human Intranet–Where Swarms and Humans Meet," *IEEE Pervasive Computing*, vol. 14, no. 1, pp. 78–83, 2015.

[2] ——, "Human-centric computing," *IEEE Transactions on Very Large Scale Integration (VLSI) Systems*, vol. 28, no. 1, pp. 3–11, 2019.

[3] S. Sen, S. Maity, and D. Das, "The body is the network: to safeguard sensitive data, turn flesh and tissue into a secure wireless channel," *IEEE Spectrum*, vol. 57, no. 12, pp. 44–49, 2020.

[4] F. Solt, R. Benarrouch, G. Tochou, O. Facklam, A. Frappé, A. Cathelin, A. Kaiser, and J. M. Rabaey, "Energy Efficient Heartbeat-Based MAC Protocol for WBAN Employing Body Coupled Communication," *IEEE Access*, vol. 8, pp. 182 966–182 983, 2020.

[5] G. Tochou, R. Benarrouch, D. Gaidioz, A. Cathelin, A. Frappe, A. Kaiser, and J. Rabaey, "A Fully-Digital 0.1-to-27 Mb/s ULV 450 MHz Transmitter with sub-100μW Power Consumption for Body-Coupled Communication in 28 nm FD-SOI CMOS," in *2021 IEEE Radio Frequency Integrated Circuits Symposium (RFIC)*. IEEE, 2021, pp. 195–198.

[6] X. Chen, J. Breiholz, F. B. Yahya, C. J. Lukas, H.-S. Kim, B. H. Calhoun, and D. D. Wentzloff, "Analysis and Design of an Ultra-Low-Power Bluetooth Low-Energy Transmitter With Ring Oscillator-Based ADPLL and 4× Frequency Edge Combiner," *IEEE Journal of Solid-State Circuits*, vol. 54, no. 5, pp. 1339–1350, 2019.

[7] Y. Shi, X. Chen, H.-S. Kim, D. Blaauw, and D. Wentzloff, "28.3 A 606μW mm-Scale Bluetooth Low-Energy Transmitter Using Co-Designed 3.5× 3.5 mm 2 Loop Antenna and Transformer-Boost Power Oscillator," in *2019 IEEE International Solid-State Circuits Conference-(ISSCC)*. IEEE, 2019, pp. 442–444.

[8] G. de Streel, F. Stas, T. Gurne, F. Durant, C. Frenkel, A. Cathelin, and D. Bol, "SleepTalker: A ULV 802.15. 4a IR-UWB transmitter SoC in 28-nm FDSOI achieving 14 pJ/b at 27 Mb/s with channel selection based on adaptive FBB and digitally programmable pulse shaping," *IEEE Journal of Solid-State Circuits*, vol. 52, no. 4, pp. 1163–1177, 2017.

[9] J. Ryckaert, G. Van der Plas, V. De Heyn, C. Desset, B. Van Poucke, and J. Craninckx, "A 0.65-to-1.4 nJ/burst 3-to-10 GHz UWB all-digital TX in 90 nm CMOS for IEEE 802.15.4a," *IEEE Journal of Solid-State Circuits*, vol. 42, no. 12, pp. 2860–2869, 2007.

[10] Y.-J. Lin, S.-Y. Park, X. Chen, D. Wentzloff, and E. Yoon, "4.32-pj/b, overlap-free, feedforward edge-combiner-based ultra-wideband transmitter for high-channel-count neural recording," *IEEE Microwave and Wireless Components Letters*, vol. 28, no. 1, pp. 52–54, 2017.

[11] Y. Park and D. D. Wentzloff, "An all-digital 12 pJ/pulse IR-UWB transmitter synthesized from a standard cell library," *IEEE Journal of Solid-State Circuits*, vol. 46, no. 5, pp. 1147–1157, 2011.

[12] P. P. Mercier, D. C. Daly, and A. P. Chandrakasan, "An energy-efficient all-digital UWB transmitter employing dual capacitively-coupled pulse-shaping drivers," *IEEE Journal of Solid-State Circuits*, vol. 44, no. 6, pp. 1679–1688, 2009.

[13] T. Norimatsu, R. Fujiwara, M. Kokubo, M. Miyazaki, A. Maeki, Y. Ogata, S. Kobayashi, N. Koshizuka, and K. Sakamura, "A UWB-IR transmitter with digitally controlled pulse generator," *IEEE Journal of Solid-State Circuits*, vol. 42, no. 6, pp. 1300–1309, 2007.

[14] T. Bos, W. Dehaene, and M. Verhelst, "Ultrasound in-body communication with OFDM through multipath realistic channels," in *2019 IEEE Biomedical Circuits and Systems Conference (BioCAS)*. IEEE, 2019, pp. 1–4.

[15] J. Yoo, "Body coupled communication: Towards energy-efficient body area network applications," in *2017 IEEE International Symposium on Radio-Frequency Integration Technology (RFIT)*. IEEE, 2017, pp. 244–246.

[16] J. Park and P. P. Mercier, "Magnetic human body communication," in *2015 37th Annual International Conference of the IEEE Engineering in Medicine and Biology Society (EMBC)*. IEEE, 2015, pp. 1841–1844.

[17] ——, "A Sub-10-pJ/bit 5-Mb/s Magnetic Human Body Communication Transceiver," *IEEE Journal of Solid-State Circuits*, vol. 54, no. 11, pp. 3031–3042, 2019.

[18] M. A. Callejon, D. Naranjo-Hernandez, J. Reina-Tosina, and L. M. Roa, "Distributed circuit modeling of galvanic and capacitive coupling for intrabody communication," *IEEE Transactions on Biomedical Engineering*, vol. 59, no. 11, pp. 3263–3269, 2012.

[19] J. Bae, H. Cho, K. Song, H. Lee, and H.-J. Yoo, "The signal transmission mechanism on the surface of human body for body channel communication," *IEEE Transactions on microwave theory and techniques*, vol. 60, no. 3, pp. 582–593, 2012.

[20] A. Thielens, R. Benarrouch, S. Wielandt, M. G. Anderson, A. Moin, A. Cathelin, and J. M. Rabaey, "A comparative study of on-body radio-frequency links in the 420 MHz–2.4 GHz range," *Sensors*, vol. 18, no. 12, p. 4165, 2018.

[21] R. Benarrouch, A. Thielens, A. Cathelin, A. Frappé, A. Kaiser, and J. Rabaey, "Capacitive Body-Coupled Communication in the 400-500 MHz Frequency Band," in *EAI International Conference on Body Area Networks*. Springer, 2019, pp. 218–235.

[22] A. Fort, C. Desset, J. Ryckaert, P. De Doncker, L. Van Biesen, and S. Donnay, "Ultra wide-band body area channel model," in *IEEE International Conference on Communications, 2005. ICC 2005. 2005*, vol. 4. IEEE, 2005, pp. 2840–2844.

[23] S. Maity, B. Chatterjee, G. Chang, and S. Sen, "BodyWire: A 6.3-pJ/b 30-Mb/s- 30-dB SIR-tolerant broadband interference-robust human body communication transceiver using time domain interference rejection," *IEEE Journal of Solid-State Circuits*, vol. 54, no. 10, pp. 2892–2906, 2019.

[24] J.-H. Lee, K. Kim, M. Choi, J.-Y. Sim, H.-J. Park, and B. Kim, "A 16.6-pJ/b 150-Mb/s body channel communication transceiver with decision feedback equalization improving¿ 200% area efficiency," in *2017 Symposium on VLSI Circuits*. IEEE, 2017, pp. C62–C63.

[25] W. Saadeh, M. A. B. Altaf, H. Alsuradi, and J. Yoo, "A 1.1-mW ground effect-resilient body-coupled communication transceiver with pseudo OFDM for head and body area network," *IEEE Journal of Solid-State Circuits*, vol. 52, no. 10, pp. 2690–2702, 2017.

[26] J. Jang, J. Lee, K.-R. Lee, J. Lee, M. Kim, Y. Lee, J. Bae, and H.-J. Yoo, "4-Camera VGA-resolution capsule endoscope with 80Mb/s body-channel communication transceiver and Sub-cm range capsule localization," in *2018 IEEE International Solid-State Circuits Conference-(ISSCC)*. IEEE, 2018, pp. 282–284.

[27] B. Chatterjee, A. Srivastava, D.-H. Seo, D. Yang, and S. Sen, "A Context-aware Reconfigurable Transmitter with 2.24 pJ/bit, 802.15. 6 NB-HBC and 4.93 pJ/bit, 400.9 MHz MedRadio Modes with 33.6% Transmit Efficiency," in *2020 IEEE Radio Frequency Integrated Circuits Symposium (RFIC)*. IEEE, 2020, pp. 75–78.

[28] B. Zhao, Y. Lian, A. M. Niknejad, and C. H. Heng, "A low-power compact IEEE 802.15. 6 compatible human body communication transceiver with digital sigma–delta IIR mask shaping," *IEEE Journal of Solid-State Circuits*, vol. 54, no. 2, pp. 346–357, 2018.

[29] H. Cho, H. Kim, M. Kim, J. Jang, Y. Lee, K. J. Lee, J. Bae, and H.-J. Yoo, "A 79 pJ/b 80 Mb/s Full-Duplex Transceiver and a 42.5μW 100 kb/s Super-Regenerative Transceiver for Body Channel Communication," *IEEE Journal of Solid-State Circuits*, vol. 51, no. 1, pp. 310–317, 2015.

[30] "IEEE Standard for Local and metropolitan area networks - Part 15.6: Wireless Body Area Networks," *IEEE Std 802.15.6-2012*, pp. 1–271, 2012.

[31] D. Marchaland, M. Villegas, G. Baudoin, C. Tinella, and D. Belot, "System concepts dedicated to UWB transmitter," in *The European Conference on Wireless Technology, 2005.* IEEE, 2005, pp. 141–144.

[32] *First Report and Order,*, document FCC 02-48, Feb. 2002.

[33] N. Cho, J. Yoo, S.-J. Song, J. Lee, S. Jeon, and H.-J. Yoo, "The human body characteristics as a signal transmission medium for intrabody communication," *IEEE transactions on microwave theory and techniques*, vol. 55, no. 5, pp. 1080–1086, 2007.

[34] S. Clerc, T. Di Gilio, and A. Cathelin, *The Fourth Terminal: Benefits of Body-Biasing Techniques for FDSOI Circuits and Systems*. Springer, 2020.

[35] M. Blagojević, M. Cochet, B. Keller, P. Flatresse, A. Vladimirescu, and B. Nikolić, "A fast, flexible, positive and negative adaptive body-bias generator in 28nm FDSOI," in *2016 IEEE Symposium on VLSI Circuits (VLSI-Circuits)*. IEEE, 2016, pp. 1–2.

[36] D. Gaidioz, M. De Matos, A. Cathelin, and Y. Deval, "Ring VCO Phase Noise Optimization by Pseudo-Differential Architecture in 28nm FD-SOI CMOS," in *2020 IEEE International Symposium on Circuits and Systems (ISCAS)*. IEEE, 2020, pp. 1–4.

[37] J. A. McNeill, "Jitter in ring oscillators," *IEEE Journal of Solid-State Circuits*, vol. 32, no. 6, pp. 870–879, 1997.

[38] S.-M. Yoo, J. S. Walling, E. C. Woo, B. Jann, and D. J. Allstot, "A switched-capacitor RF power amplifier," *IEEE Journal of Solid-State Circuits*, vol. 46, no. 12, pp. 2977–2987, 2011.

[39] G. Tochou, A. Cathelin, A. Frappé, A. Kaiser, and J. Rabaey, "Impact of Forward Body-Biasing on Ultra-Low Voltage Switched-Capacitor RF Power Amplifier in 28 nm FD-SOI," *IEEE Transactions on Circuits and Systems II: Express Briefs*, 2021.

[40] G. Tochou. RFIC Industry Showcase - IMS 2021, . June 14, 2021. [Online]. Available: https://ieeetv.ieee.org/channels/mtts/guillaume-tochou-rfic-industry-showcase-ims-2021

[41] J. M. Rabaey, A. C. Arias, and R. Muller, "Architecting the human intranet," in *ESSCIRC 2021-IEEE 47th European Solid State Circuits Conference (ESSCIRC)*. IEEE, 2021, pp. 15–20.

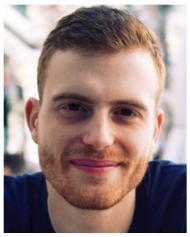

Guillaume Tochou (Graduate Student Member, IEEE) received the B.S. and M.S. degrees in electrical engineering from Grenoble INP Phelma, France, in 2016 and 2018, respectively. He is currently pursuing the Ph.D. degree with STMicroelectronics and the University of Lille 1, France, through a CIFRE program. As part of the Ph.D. degree, he has been a Visiting Student Researcher with the Berkeley Wireless Research Center (BWRC), University of California, Berkeley. He received the Best Industrial Paper Award at IEEE RFIC 2021. His research interests focus on ultra-low power wireless communication for the IoT and body area network applications.

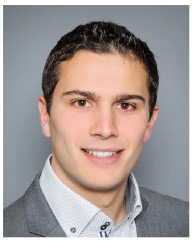

Robin Benarrouch (Member, IEEE) received the B.S. and M.S.Eng. degrees in electrical engineering from CPE Lyon, France, in 2013 and 2015, respectively, and the M.Res. degree in electronics and embedded system from INSA Lyon, Centrale Lyon, UCBL, France, in 2015. He received the Ph.D. degree in 2021 from the University of Lille 1, France, under a CIFRE program with STMicroelectronics. He conducted half of his research as a Visiting Scholar Researcher with the Berkeley Wireless Research Center (BWRC), University of California Berkeley, Berkeley, USA. He currently is a system engineer at STMicroelectronics. His interests include signal processing and system architecture on low power UWB wireless communication for IoT and BAN applications.

David Gaidioz (Member, IEEE) received the B.S. and M.S.Eng. degrees in electrical engineering from Bordeaux INP ENSEIRB-MATMECA, France, in 2014 and 2016, respectively. He received the Ph.D. degree in 2021 from the University of Bordeaux, France, under a CIFRE program with STMicroelectronics. He is currently a R&D engineer at STMicroelectronics. His research interests include frequency synthesis and low power wireless communications for the IoT and RFIC design.

Andreia Cathelin (Senior Member, IEEE) started electrical engineering studies at the Polytechnic Institute of Bucarest, Romania and graduated with MS from the Institut Supérieur d'Electronique du Nord (ISEN), Lille, France in 1994. In 1998 and 2013 respectively, she received PhD and "habilitation à diriger des recherches" (French highest academic degree) from the Université de Lille 1, France. Since 1998, she has been with STMicroelectronics, Crolles, France, now Technology R&D Fellow. Her focus areas are in the design of RF/mmW/THz and ultra-low-power circuits and systems. She is the key design scientist in the promotion of all advanced CMOS technologies developed in the company. She is leading and driving research in advanced topics inside the company R&D program and through leadership cooperation with major universities around the world. She has also management activities as being in charge of the ST-CMP operation (the CMP is an independent organization offering small series foundry services for SME and research institutes). Andreia is very active in the IEEE community since more than 15 years, strongly implied with SSCS and its Adcom, the Executive Committee of VLSI Symposium and has been the TPC chair of ESSCIRC 2020 and 2021 in Grenoble. She has been for 10 years involved with ISSCC as RF subcommittee chair and then member of the Executive Committee. She is as well a founding member of the IEEE SSCS Women in Circuits group. Andreia has authored or co-authored 150+ technical papers and 14 book chapters, has co-edited the Springer book "The Fourth Terminal, Benefits of Body-Biasing Techniques for FDSOI Circuits and Systems" and has filed more than 25 patents. Andreia is a co-recipient of the ISSCC 2012 Jan Van Vessem Award for Outstanding European Paper and of the ISSCC 2013 Jack Kilby Award for Outstanding Student Paper. She is as well the winner of the 2012 STMicroelectronics Technology Council Innovation Prize, for having introduced on the company's roadmap the integrated CMOS THz technology for imaging applications. Very recently, Andreia has been awarded an Honorary Doctorate from the University of Lund, Sweden, promotion of 2020.

Antoine Frappé (Senior Member, IEEE) graduated from the Institut Supérieur d'Electronique du Nord (ISEN), Lille, France in 2004. He received the M.Sc., Ph.D., and HDR (French highest academic degree) in electrical engineering from the University of Lille, France in 2004, 2007, and 2019, respectively. Since 2004, he is a member of the Silicon Microelectronics group at the Institute of Electronics, Microelectronics, and Nanotechnologies (IEMN) in Villeneuve d'Ascq, France. He obtained a Fulbright grant in 2008 to pursue research in communication systems at the Berkeley Wireless Research Center (BWRC) at UC Berkeley, CA, USA. He is now an Associate Professor at Junia ISEN, Lille, France, leading the Electronics Team. His research interests concern digital RF transmitters, high-speed converters, mixed-signal design for RF and mmW communication systems, energy-efficient integrated systems, event-driven and neuro-inspired circuits for embedded machine learning. He was a co-recipient of a Best Student Paper Award at the 2011 Symposium on VLSI Circuits, a Best Paper Award at the 2020 IEEE AICAS Conference, and an Industrial Best Paper Award at the 2021 IEEE RFIC Symposium. He plays an active role as a board member of the France Section of the IEEE Circuits and Systems Society and Counselor of the IEEE Lille Student Branch.

Andreas Kaiser (Senior Member, IEEE) received the engineering diploma from the Institut Supérieur d'Electronique du Nord (ISEN), Lille, France, in 1984, and the PhD and HDR degrees in 1990 and 1998 respectively from the University of Lille. In 1990 he joined the Centre National de la Recherche Scientifique (CNRS) where he was responsible for the analog/RF IC design group at the Institut d'Electronique, de Microelectronique et de Nanotechnologies (IEMN) in Lille. He has been the co-director of the IEMN-STMicroelectronics Common Lab from 2002 until 2012. From 2012 until 2017 he has been the Dean of the JUNIA-ISEN Engineering faculty. He is now scientific director at the JUNIA engineering graduate school. His research interests are continuous and discrete time analog circuits, data-converters, analogue design automation, RF-MEMS and RF circuits. Prof. Kaiser served as TPC Chair of the European Solid State Circuits Conference in 1995 and 2005 and has been a guest and associate editor to the IEEE Journal of Solid State Circuits. He has been the advisor of 38 completed PhDs, has published more than 160 publications in peer-reviewed journals and conferences and holds 17 patents.

Jan Rabaey (Life Fellow, IEEE) is a Professor in the Graduate School in the EECS Department the University of California at Berkeley, after being the holder of the Donald O. Pederson Distinguished Professorship at the same institute for over 30 years. He is a founding director of the Berkeley Wireless Research Center (BWRC) and the Berkeley Ubiquitous SwarmLab, and has served as the Electrical Engineering Division Chair at Berkeley twice. In 2019, he also became the CTO of the System-Technology Co-Optimization (STCO) Division of IMEC, Belgium. Prof. Rabaey has made high-impact contributions to a number of fields, including low power integrated circuits, advanced wireless systems, mobile devices, sensor networks, and ubiquitous computing. His current interests include the conception of the next-generation distributed systems, as well as the exploration of the interaction between the cyber and the biological worlds. He is the recipient of numerous awards, is a Life Fellow of the IEEE, and has been involved in a broad variety of start-up ventures.